Fast Antenna Characterization Improvement by Pattern Rotations

Nicolas Mezieres, Benjamin Fuchs, Laurent Le Coq, Jean-Marie Lerat, Romain Contreres, Gwenn Le Fur

Fast Antenna Characterization Improvement by Pattern Rotations

Nicolas Mézières, Benjamin Fuchs, Laurent Le Coq, Jean-Marie Lerat, Romain Contreres and Gwenn Le Fur

***Abstract*—A post-processing procedure is proposed to improve the characterization of antenna patterns from a small number of field samples. By appropriately rotating the measured pattern of the antenna under test, the sparsity of its spherical harmonic spectrum can be enhanced. Our procedure enables extracting as much information as possible from a given measurement dataset and leads to a notable improvement of the antenna radiation pattern reconstruction accuracy. The best orientation of the antenna is found by testing a reduced set of angles and using Gaussian processes as interpolation approach. This post-processing requires no modification of the measurement procedure and therefore no extra measurement time. The improved fast antenna characterization accuracy is validated on both spherical near and far-field simulations and measurements for various types of antennas and compared with the state-of-the-art approach.**

***Index Terms*—Antenna measurements, antenna radiation patterns, compressed sensing, sparse recovery, spherical wave expansion**

I. Introduction

THE spherical antenna measurement technique is a standard and efficient tool for both near and far-field characterization. The number of field sampling points grows quadratically with respect to the largest electrical dimension ka of the Antenna Under Test (AUT) [1], k being the wavenumber and a the radius of the minimal sphere enclosing the antenna (illustrated in Fig. 1), involving large and possibly prohibitive measurement times. Recently, the exploitation of the sparse expansion of the field radiated by antennas into spherical harmonic basis has been shown to greatly reduce the number of required field samples, leading to important decreases in field acquisition duration, as shown in [2]–[6]. They enable a very good approximation of the radiation pattern from half of the field samples required by well established standard technique using a first order probe and an equiangular sampling [1], [7]. The expansion of the antenna radiated field into the Vector Spherical Harmonic (VSH) basis depends on the chosen coordinate system. Indeed, the radiation pattern of an infinitesimal electric dipole oriented in the $\hat{z}$ direction can be described using only one VSH, any other orientation will require at least two VSH. Consequently, one can legitimately wonder how to choose the coordinate system yielding the sparsest field expansion. This very point has been addressed by [3], where an iterative algorithm is proposed to increase the sparsity of the expansion by rotations and translations. To our best knowledge, this is the only work where the AUT orientation is optimized to this end. We refer to this work, taken as reference for comparisons, as State-Of-the-Art (SOA) in the sequel. Let us point out that the translation of the coordinate system also leads to a change in the total number of VSH, as shown in [8]–[10], whereas rotations only modify the number of significant ones.

This paper proposes a post-processing procedure to efficiently rotate the measured pattern of the AUT in order to make its spherical harmonic spectrum as sparse as possible. To do so, the sparsity of the VSH spectrum is computed for a limited number of rotation angles taken on a coarse grid. Then the spectrum sparsity is estimated over the whole research domain using Gaussian Processes (GP). The method is validated on near-field using simulation data and on far-field using experimental data.

The paper is organized as follows. The spherical harmonic expansion of the electric field is reviewed in Section II. The identification of the sparse spherical harmonic coefficients and metrics are also detailed. The proposed procedure to rotate the antenna pattern in order to achieve a sparser field expansion is described in Section III. This technique is validated over near-field simulation data and over far-field experimental data in Sections IV and V respectively. Conclusions and perspectives are drawn in Section VI.

II. Fast Antenna Measurements

A. Spherical Harmonic Expansion

The electric field $\mathbf{E}(r,\theta,\varphi)$ in spherical coordinates radiated outside the sphere enclosing all sources can be expanded into the VSH basis as follows [1]:

$$\mathbf{E}(r,\theta,\varphi) = \frac{k}{\sqrt{\eta}} \sum_{s=1}^{2} \sum_{n=1}^{\infty} \sum_{m=-n}^{n} Q_{smn} \mathbf{F}_{smn}(r,\theta,\varphi) \qquad (1)$$

where η is the admittance of the propagation medium, Q_{smn} are the spherical coefficients and $\mathbf{F}_{smn}$ the VSH functions. To formalize the problem, the directions (θ,φ) are discretized and the infinite series in (1) is truncated to $N = \lfloor ka \rfloor + 10$ [1], and $\lfloor x \rfloor$ is the greatest integer less than or equal to x. After discretization of the directions (θ,φ) and for a fixed distance r, the expansion (1) can be expressed as a linear system : $\mathbf{y} = \mathbf{A}\mathbf{x}$ where the vector $\mathbf{x}$ of size N_c contains the spherical coefficients Q_{smn}. The vector $\mathbf{y}$ of size M gathers the values of the measured electric field, $\mathbf{y}_j = \mathbf{E}(\theta_j,\varphi_j)$ where (θ_j,φ_j) are the sampling positions over the sphere. The matrix $\mathbf{A}$ corresponds to the harmonics $\mathbf{F}_{smn}$, each column being associated to a triplet (s,m,n) and each row to a position (θ_j,φ_j).

Manuscript received xx, 2020; revised xx, xx.

This work was carried out in the frame of a CNES and LNE grant and is supported in part by the European Union through the European Regional Development Fund (ERDF), and by the french region of Brittany, Ministry of Higher Education and Research, Rennes Métropole and Conseil Départemental 35, through the CPER Project SOPHIE / STIC & Ondes.

N. Mézières is with IETR, CNES and LNE (e-mail: nicolas.mezieres@univ-rennes1.fr). B. Fuchs and L. Le Coq are with the IETR, UMR CNRS 6164, Rennes. J.-M. Lerat is with the LNE, Trappes. R. Contreres and G. Le Fur are with the CNES, Toulouse.

Digital Object Identifier

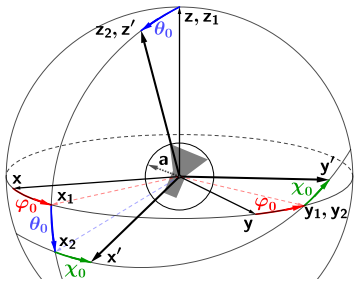

Fig. 1. Euler's angles in zyz convention. Three rotations of angles $(\varphi_0, \theta_0, \chi_0)$ with respect to the axis $\mathbf{z}, \mathbf{y}_1, \mathbf{z}_2 = \mathbf{z}'$ enables to go from the basis $\{\mathbf{x}, \mathbf{y}, \mathbf{z}\}$ to $\{\mathbf{x}', \mathbf{y}', \mathbf{z}'\}$. The radius of the minimum enclosing sphere around the antenna is denoted a. The intermediate basis $\{\mathbf{x}_1, \mathbf{y}_1, \mathbf{z}_1\}$ and $\{\mathbf{x}_2, \mathbf{y}_2, \mathbf{z}_2\}$ are also displayed.

The electric near and far-field radiated by the AUT can both be expanded according to (1). In the near-field case, the radiation pattern of the probe has to be taken into account, which leads after some manipulations to the transmission formula and specific considerations, as detailed in [1], [7].

B. Sparse Expansion of the Field

The field acquisition time is tied to the number of sampling points required. By leveraging the sparsity of the spherical coefficients $\mathbf{x}$, their identification can be achieved by solving an underdetermined linear system, thus we are able to decrease the size of the measurement set. A possible way is then to consider the following optimization problem, known as Basis Pursuit DeNoising (BPDN) [11]:

$$\min_{\mathbf{x}} \|\mathbf{x}\|_1 \text{ subject to } \|\mathbf{A}\mathbf{x} - \mathbf{y}\|_2 \leq \sigma \tag{2}$$

where $\sigma > 0$ controls the fitting to the data contained in $\mathbf{y}$ and is known as error tolerance. The tuning of this quantity has been considered in [6]. BPDN problem (2) is a specific convex optimization problem, belonging to sparse recovery category. It can be solved efficiently using many readily available routines, such as the SPGL1 algorithm [12], [13].

C. Fast Antenna Measurement Performances

1) Effective Sparsity and Field Comparison: The sparsity of a signal can be measured by counting the number of non-zero coefficients. However, real-world data are always noisy and low magnitude coefficients are often not relevant. To this end, we define the notion of effective sparsity denoted k_T, giving the number of significant coefficients with respect to a chosen threshold T (in dB), as

$$k_T(\mathbf{x}) = \frac{1}{N_c} \, \# \left\{ \frac{|\mathbf{x}_j|}{\|\mathbf{x}\|_\infty} > 10^{\frac{T}{20}}, j = 1, \ldots, N_c \right\} \tag{3}$$

with $\#$ the cardinal operator and $\|\mathbf{x}\|_\infty$ the maximum magnitude of $\mathbf{x}$'s components. An effective sparsity k_{-40} means that only the coefficients greater than $-40\,\mathrm{dB}$ from the maximum magnitude one count as non-zero. Truncating the spherical spectrum with respect to this threshold leads to negligible changes in the radiation pattern [6].

To assess the performance of a given field reconstruction, we compare the reconstructed field $\widetilde{\mathbf{y}}$ to the reference one, $\mathbf{y}$. For that purpose, the Equivalent Error Signal metric (EES) returns a mean relative error in dB contained in $\widetilde{\mathbf{y}}$ with respect to the reference $\mathbf{y}$, both of size M, and is defined as

$$\mathrm{EES}(\mathbf{y}, \widetilde{\mathbf{y}}) = 20 \log_{10} \left(\frac{\|\mathbf{y} - \widetilde{\mathbf{y}}\|_1}{M \|\mathbf{y}\|_\infty} \right). \tag{4}$$

2) Phase Transition Diagrams (PTD): These diagrams [14] are an efficient way to display the probability of success of sparse recovery problems such as (2). This probability depends on the number of non-zero components of the solution and the sampling ratio, which is the number of data over the number of unknowns. The behaviour of a typical PTD is illustrated in Fig. 2. They can also be used to access the recovery success of fast antenna measurement procedures, as shown in [2], [4]–[6]. The transition between a failed and successful identification of the sparse solution is very steep, meaning that only a few additional measurements may be required to go from a failed to a correct identification. Intuitively, a small number of non-zero coefficients can be correctly retrieved from only a few measurement samples. Consequently, to properly characterize the field radiated by a given antenna, the sparser its spherical harmonic spectrum, the smaller the number of required field samples.

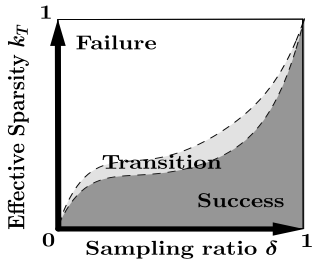

Fig. 2. Phase Transition Diagram sketch with its three regions : failure, transition and success of the spherical coefficients identification as a function of their effective sparsity and the sampling ratio δ, i.e. the number of field samples over the number of coefficients.

3) Spectrum Sparsity and Reconstruction Accuracy: Following the PTD theory, we generate random spherical coefficients sets according to a normal law with predetermined variance with a given effective sparsity k_{-40}. We emulate realistic antenna patterns by drawing random spherical coefficients spectrum and try to retrieve them using BPDN.

The accuracy of reconstruction is given by the EES metric (4) between the field computed from the random set, which is our reference $\mathbf{y}$, and the interpolated one from a coarse sampling, $\widetilde{\mathbf{y}}$. As shown in Fig. 3, a lower effective sparsity (or equivalently less significant coefficients) leads to better EES values. The EES metric defined in (4) represents a mean error. Hence, a modification of only $1\,\mathrm{dB}$ may already represents a lot of changes and accuracy gain/loss, especially if they accumulate over some area. However, these random coefficients spread almost evenly amongst the spectrum but undersampling conditions will make the fast variations, or equivalently the spherical modes with large n and/or m harder to be identified.

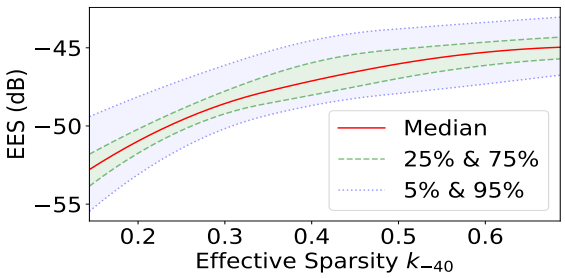

Fig. 3. Quantiles of the EES (extracted from 100 trials) as a function of the effective sparsity for a fixed number of data (2352 data for 3360 spherical coefficients, sampling ratio $\delta = 70\,\%$).

III. Rotations for Sparser Field Expansion

An approach is proposed to make the spherical harmonic spectrum of the AUT sparser and therefore to improve, for a given field sampling, the accuracy of a fast antenna measurement. The rotation of the AUT changes its spherical harmonic spectrum. We exploit this property to minimize the number of modes required to describe the AUT pattern. A procedure based on GP interpolation is proposed to find the rotation angles achieving the sparsest AUT spectrum.

A. Coordinate System Rotation

A common way to represent rotations in 3D space is to use Euler's angles $(\varphi_0, \theta_0, \chi_0)$. The zyz convention, used in [1], is illustrated in Fig. 1 for positives angles $(\varphi_0, \theta_0, \chi_0)$. The basis $\{\mathbf{x}', \mathbf{y}', \mathbf{z}'\}$ is obtained from the initial one $\{\mathbf{x}, \mathbf{y}, \mathbf{z}\}$ by three successive rotations of angles φ_0, θ_0 and χ_0. We can express the spherical harmonics $\mathbf{F}_{smn}(\mathbf{r})$ in the first system $\{\mathbf{x}, \mathbf{y}, \mathbf{z}\}$ as a linear combination (depending on Euler's angles) of the ones in the rotated system, $\{\mathbf{x}', \mathbf{y}', \mathbf{z}'\}$ with the (small) d-Wigner function [15], namely $\mathbf{F}_{s\mu n}(\mathbf{r}')$ as follows [1]:

$$\mathbf{F}_{smn}(\mathbf{r}) = \sum_{\mu=-n}^{n} e^{im\varphi_0} d^n_{\mu m}(\theta_0) e^{i\mu\chi_0} \mathbf{F}_{s\mu n}(\mathbf{r}'). \tag{5}$$

B. Problem Formulation

Our goal is to find the rotation angles $(\varphi_0, \theta_0, \chi_0)$ leading to the sparsest VSH representation of the field radiated by the AUT. The rotation angle φ_0 only introduces a phase shift according to (5), and thus does not influence the sparsity of the spectrum. Therefore, only the couple of rotation angles (θ_0, χ_0) have to be determined. After rotations with angles (θ_0, χ_0), the equation satisfied by the radiated field reads :

$$(\mathbf{A}\mathbf{R}_{\theta_0,\chi_0})\mathbf{x}(\theta_0, \chi_0) = \mathbf{y} \tag{6}$$

where $\mathbf{R}_{\theta_0,\chi_0}$ is the matrix encoding the rotation of the VSH, described in (5) for the couple (θ_0, χ_0). We then solve :

$$\min_{\mathbf{x}} \|\mathbf{x}\|_1 \text{ subject to } \|\mathbf{A}\mathbf{R}_{\theta_0,\chi_0}\mathbf{x} - \mathbf{y}\|_2 \leq \sigma \tag{7}$$

We evaluate the effective sparsity k_{-40} defined in (3) of the solution $\mathbf{x}(\theta_0, \chi_0)$ using only the two rotation angles (θ_0, χ_0). The computation of $\mathbf{R}_{\theta_0,\chi_0}$ takes about 1.5 s and the resolution of (7) using SPGL1 takes about 1.2 s for a matrix $\mathbf{A}$ of size 2522×4606 with an Intel i7-8700 and 16 GB RAM, i.e. solving the BPDN problem is not as time consuming as computing the VSH rotation matrix. However, testing a lot of couples (θ_0, χ_0) may become a heavy computational task. To avoid that difficulty, the effective sparsity k_{-40} of the solutions is estimated from a coarse (θ_0, χ_0) grid using GP and a relevant restriction of the research domain.

The SOA method [3] proposes to find $\mathbf{x}(0, 0)$ before optimizing over the three Euler's angles by minimizing $\|\mathbf{R}_{\varphi_0,\theta_0,\chi_0}\mathbf{x}(0, 0)\|_1$. Note that this problem is much harder than minimizing $\|\mathbf{T}\mathbf{x}\|_1$ for a given matrix T, as it cannot be casted into a convex optimization problem. Iterative minimization methods, such as gradient descent, may be trapped in local minima and will require around as much matrix computation as parameters to optimize. The optimization has to be done for several initialization points and the final result may not the be the true minimum.

C. Effective Sparsity Estimation via Gaussian Processes

1) Interpolation: GP are stochastic processes that can be used to interpolate continuous functions. They are well adapted to situations where evaluating the function is computationally heavy. GP have already shown a great relevance in many applications and motivated a lot of research [16]. They enable the computation of confidence intervals and parameters tuning for better estimation depending on the fed data. Rotation of the VSH basis can be seen as the rotation of the AUT into the new coordinate system. Physically, it represents a continuous modification of the field, and thus of its spectrum. The function $k_T(\mathbf{x}(\theta_0, \chi_0))$ can consequently be fairly well approximated by a continuous function, as shown in Fig. 4. The region with the lowest sparsity is indeed well identified with a few samples. In this case, the SOA method detects a sparsity minimum but the minimization of $\|\mathbf{R}_{\varphi_0,\theta_0,\chi_0}\mathbf{x}(0, 0)\|_1$ does not lead to the correct Euler's angles, this will be further discussed in Section V-C.

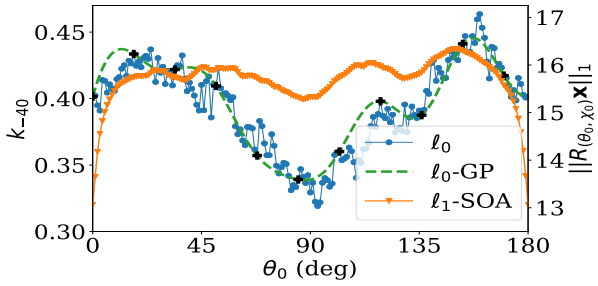

Fig. 4. Effective sparsity k_{-40} for $\chi_0 = 0°$, containing the lowest sparsity on the research domain, its GP estimation and the ℓ_1 norm found by the SOA method of the spherical coefficients for the 12 GHz reflectarray measurement. The GP curve is derived from the discrete set of values represented by black markers. The ℓ_1 only reaches a local minimum.

The objective is to interpolate the effective sparsity function $k_T(\mathbf{x}(\theta_0, \chi_0))$ from a reduced number of values, at points $(\theta_0^{(p)}, \chi_0^{(p)})$. The interpolation $\widetilde{k}_T$ is therefore an estimation.

2) Practical Implementation: A GP is characterized by its expectancy, set to 0 in our case, and its covariance, or kernel function, $\mathbb{V}$. We let $\mathbb{V}(\mathbf{a}_1, \mathbf{a}_2) = h(\|\mathbf{a}_1 - \mathbf{a}_2\|) =$

$\exp(-\frac{\|\mathbf{a}_1-\mathbf{a}_2\|^2}{2l^2})$, where $\|\cdot\|$ is the Euclidean norm and l a positive parameter characterizing the distance at which points influence themselves. This kernel is named square exponential and is known to produce indefinitely differentiable curves [16]. If $\mathbf{a} = (\theta_0, \chi_0)$ and the known values of k_T are located at points $\mathbf{a}^{(p)} = (\theta_0^{(p)}, \chi_0^{(p)}), p \in \{1, \dots, P\}$, then if $\mathbf{K}$ is the vector gathering the $k_T(\mathbf{a}^{(p)})$:

$$\widetilde{k}_T(\mathbf{x}(\mathbf{a})) = \left[\mathbb{V}(\mathbf{a}, \mathbf{a}^{(1)}) \ \dots \ \mathbb{V}(\mathbf{a}, \mathbf{a}^{(P)})\right] \mathbf{V}^{-1}\mathbf{K} \quad (8)$$

where $\mathbf{V} = (v_{lm})$ is the matrix containing the covariance between the data points $\mathbf{a}^{(i)}$, i.e. $v_{lm} = \mathbb{V}(\mathbf{a}^{(l)}, \mathbf{a}^{(m)})$. Once the values k_T are known at some points, evaluating $\widetilde{k}_T$ can be done by small scale matrix multiplications, allowing a lot of fast optimization techniques.

3) Research Domain and Testing Grid: The initial domain of (θ_0, χ_0) is $[0, 180] \times [0, 360]$ in degrees. However, thanks to the symmetries of the VSH, it can be reduced to $(\theta_0, \chi_0) \in [0, 180[\times[0, 90[$. First, the case $\theta_0 = 0°$, or 180° by symmetry, has to be computed once, because it only induces a phase shift of the coefficients. Secondly, a first known rotation in χ_0 can be applied to ensure that the main beam of the field can be sent to one of the pole or to achieve symmetry with respect to the plane $x = 0$. The number of tested points has been chosen empirically and these points are regularly spaced on a testing grid with a step of 17°, allowing to capture the global behaviour of the effective sparsity, as shown in Fig. 4. It implies 61 BPDN problems to solve and rotations matrix to compute, 6 different χ_0 values for ten θ_0 values plus one at $\theta_0 = 0°$. Finally, we have set l, the characteristic length of the GP introduced in the previous paragraph to 22.5°, which is between 17° and $17\sqrt{2} \approx 24°$, respectively the length of the edge or the diagonal of a cell of the testing grid.

IV. Validation on Antenna Spherical Near-Field Simulation

A. Methodology

An antenna is modelled numerically using HFSS and its near-field over an equiangular sampling scheme, $\delta\varphi = \delta\theta = 2°$ (where $\delta\varphi$ and $\delta\theta$ are the angular steps in φ and θ respectively) over the full sphere is exported, constituting the reference data set. A coarse sampling over the sphere using an *igloo* sampling strategy [4] is selected from it. It is defined as $\delta\varphi = \frac{\delta\theta}{\sin\theta}$. A low density sampling is chosen to mimic a fast measurement data set, and used to compute spherical coefficients with or without rotations, using BPDN (2).

B. Waveguide Array at 50 GHz

The presented case is a linear array of waveguides constituted by 13 elements with 3 mm spacing at 50 GHz (same excitation magnitude but different phases), with an enclosing sphere of radius a =25 mm, hence a truncation order $N = 36$ (or $N_c = 2736$ coefficients). The dense sampling rate for far-field reference has 6152 samples, while the low density one, used for sparse recovery, has only 1876. The measurement coordinate system $(\mathbf{x}, \mathbf{y}, \mathbf{z})$ does, on purpose, not correspond to the symmetry of the array. Spherical coefficients with and without rotation found by GP interpolation are shown in Fig. 5. Estimated optimized rotations angles are $\theta_0 = 45°$ and $\chi_0 = 55°$. We observe that raw data produces some high frequency modes which are not physically realistic and are due to the too low density sampling rate. The optimized rotation reduces the number of significant spherical coefficients and consequently vanishes the high frequency modes. Reference far-field is illustrated in Fig. 6 with a specific cutting plane. The effective sparsities are $k_T = 33\,\%$ and $15\,\%$ for the raw and rotated field respectively with corresponding EES values -36.6 dB and -53.4 dB.

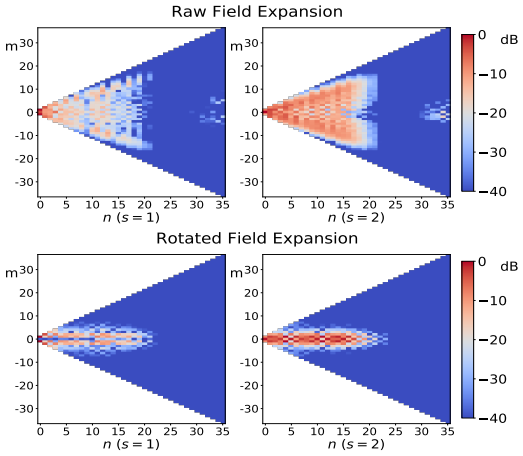

Fig. 5. Normalized spherical coefficients of the waveguide array simulated at 50 GHz.

V. Validation on Antenna Far-Field Measurement

We now validate the procedure using antenna far-field measurements. Three antennas are investigated : a Luneburg lens, a Radiating Cavity Antenna (RCA) and a ReflectArray (RA). The Table I gathers information about the presented cases in this section. For each antenna, we show a cartography of the pattern and the position of the optical axis $\mathbf{z}'$ of the optimized rotated coordinate system, they are presented in Fig. 7. The reconstruction results are reported in Table II.

TABLE I
Characteristics of the Investigated Antennas

Antenna	Size a(m)	Coef. N_c	Meas. set	Subsample
Lens 12 GHz	0.15	4606	9746	3702
RCA 6 GHz	0.13	1456	2332	1088
RA 12 GHz	0.15	4606	10970	2628

A. Methodology

All measurements have been carried out in the two far-field anechoic chambers of the M^{2}ARS facilities at IETR. Both are equipped with a roll-over-azimuth positioning system and a mechanical probe polarization change. The field is acquired step by step with a high density sampling rate following an *igloo* strategy to avoid the oversampling near the poles, $\delta\varphi = \frac{\delta\theta}{\sin\theta}$, providing our reference patterns. As in near-field in IV-A, we select a coarse *igloo* sampling to mimic

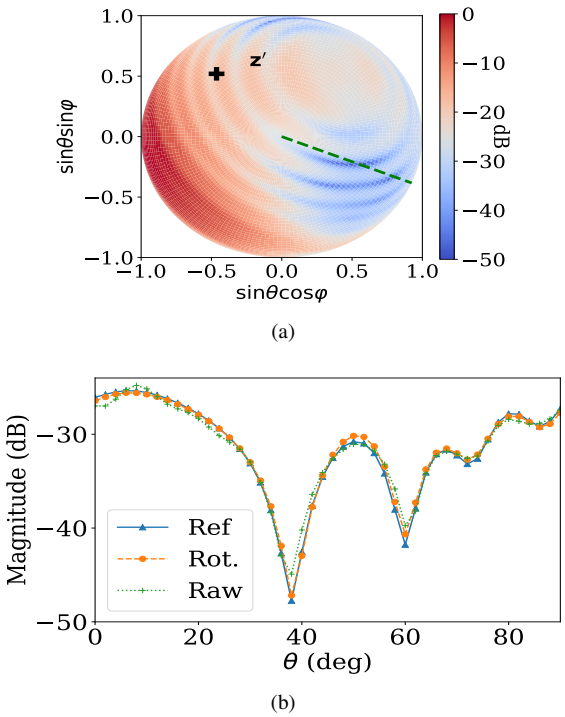

(a)

(b)

Fig. 6. Normalized electric far-field radiated by the waveguide array at 50 GHz ($\mathbf{z}'$ chosen by GP) in (a) and the cutplane represented by the green doted line in (b).

a fast measurement data set. The resulting interpolating field is derived by spherical coefficients identified by BPDN and compared with the reference pattern. The GP interpolation is done with the same parameters as in near-field.

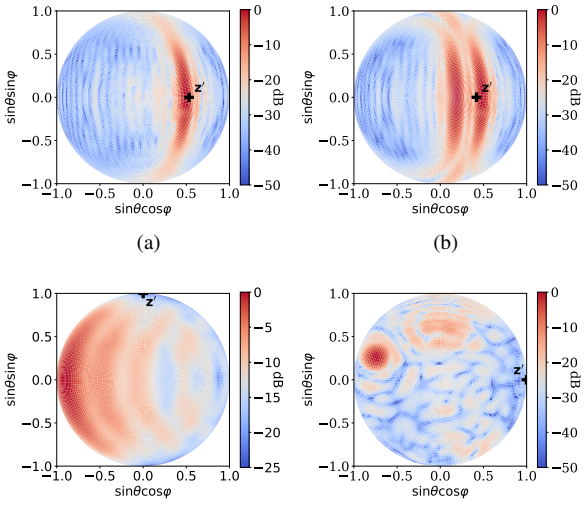

(a) (b)

(c) (d)

Fig. 7. Normalized electric far-fields radiated by: (a) the single beamed Luneburg lens at 12 GHz, (b) the dual beamed version, (c) the radiating cavity antenna at 6 GHz and (d) the reflectarray at 12 GHz. Cross markers $\mathbf{z}'$ are the position of the z-axis after the optimized rotation by Gaussian processes.

B. Experimental cases

1) Luneburg Lens Antenna at 12 GHz*:* The flat Luneburg lens antenna is fed by several waveguides [17] and measured over the full sphere. We investigate two configurations : one excited waveguide generating one beam and two excited waveguides radiating two beams. The resulting reference far-fields are shown in Fig. 7a and 7b.

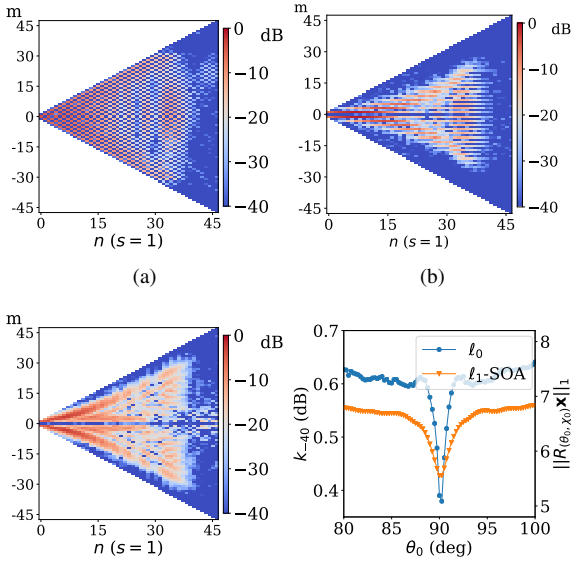

(a) (b)

(c) (d)

Fig. 8. Normalized spherical coefficients for $s = 1$ of the Luneburg Lens with single beam for the angles found by the SOA method in (a), the proposed approach in (b) and default position in (c). The curves generated by the SOA method and the corresponding effective sparsity in the $\chi_0 = 90°$ plane is shown in (d).

2) Lens with single Beam : The 3D far field pattern is displayed in Fig. 7a. We note that the procedure chooses to orientate the z'-axis at the maximum of the field. Spherical coefficients are displayed in Fig. 8b, we clearly observe less significant coefficients for the rotated field expansion with the proposed approach. The result of the SOA method is different. The rotation is done so a symmetry with respect to the equator of the radiation pattern is achieved, explaining the peculiar pattern in Fig. 8a, this is further discussed in Section V-C.

3) Lens with dual Beam: We generate this case from two single beam measurements. The radiation pattern is shown in Fig. 7b. The two beams nearly have the same magnitude, and the z'-axis is not located at a maximum magnitude point anymore. Hovewer, the SOA methodreturns the same result as the single beam case for the same reason.

4) Radiating Cavity Antenna at 6 GHz*:* The AUT is measured over the full sphere and is designed for Car 2 X (C2X) communications. The reference electric far-field is illustrated in Fig. 7c. This antenna has a small dynamic range, as the measured magnitudes of the electric far-field vary from 0 to -25 dB. The best rotation angles determined by GP, indicated by the cross marker in Fig. 7c, are the same as the SOA method. After performing this rotation, the number of significant coefficients is halved, as shown in Table II.

5) Reflectarray at $12\,\mathrm{GHz}$*:* The field of the reflectarray is illustrated in Fig. 7d. It has a very directive pattern with a tilted beam and the measurement is carried out over an hemisphere.

C. Discussion

1) Reconstruction accuracy: In all cases, the sparsity of the spherical coefficients is increased or equaled with respect to the SOA method. This enhanced sparsity leads to an improvement of the field reconstruction as illustrated by the values of EES in Table II. The choice of rotation angles is not trivial for most cases and cannot be guessed in advance, as shown by the $\mathbf{z}'$ markers in the far-field mappings in Fig. 7.

2) Impact of the mode distribution: Rotating the radiated field by the single beam lens at $12\,\mathrm{GHz}$ in Fig. 7a by $(\varphi_0, \theta_0, \chi_0) = (0, 90, 90)$ in degrees will put the main beam orthogonal to the equator. In such configuration, the field is symmetric with respect to it and the spherical spectrum is concentrated in the modes $\mathbf{F}_{smn}$ such that $m+n$ is even and sparsity is greatly promoted, explaining the specific pattern shown in Fig. 8a. This is achieved at a cost of pushing some modes to higher order ones (further from the line $m = 0$), which are harder to identify with undersampled sets. As shown in Fig. 8d, this case will lead to a sudden effective sparsity variation, which is well identifiable using our approach. For the RCA case, both methods chose to achieve a symmetry with respect to the equator. However, due to the small directivity of the pattern, shown in Fig. 7c, there is no creation of high order modes as in the previous case.

Considering the reflectarray case, as illustrated in Fig. 4, the SOA method fails to detect the rotation angles leading to the sparsest expansion in this case. This can be explained by the relatively low number of samples with respect to the number of unknowns since this method optimizes the rotation using the spherical coefficients found along the default orientation.

3) Computation Time: The computation time is difficult to estimate for the SOA method. Indeed, several initialization points must be tested to ensure a proper optimization, it requires multiple rotation matrix computation per iteration, being at least as costly as solving the BPDN with SPGL1, and convergence speed is highly dependent on parameter tuning, which is no trivial matter. The proposed approach always took less than 3 minutes of computation time for the configuration given in Section III-B for the largest antenna in electrical size.

4) Minimization Efficiency: The angular distance between our procedure and a brute force approach (successive refinements of a dense testing grid around the expected minima up to $0.2°$) of the optimized rotation angles is lower than $2.5°$ for all the presented measurements. The corresponding effective sparsities k_{-40} and EES values show differences of $2\ \%$ and $0.14\ \mathrm{dB}$ in the worst case.

TABLE II
EES VALUES, CORRESPONDING EFFECTIVE SPARSITIES k_{-40}

	k_{-40} (%)			EES (dB)		
Antenna	Raw	SOA	GP	Raw	SOA	GP
Lens (single)	62	43	41	-46.9	-50.0	-51.2
Lens (double)	58	37	37	-43.6	-48.3	-49.3
RCA	33	15	15	-37.2	-39.0	-39.1
RA	40	40	29	-48.0	-48.0	-50.9

VI. Conclusion

An efficient procedure using rotations of the measured antenna patterns for generating a sparser expansion of the field has been proposed. This post-processing method is valid for spherical near and far-field antenna characterization with low sampling rates and involves no extra measurement time or modification to the previous measurement procedures. It allows to exploit at best the information contained in a given undersampled field dataset. In addition, the proposed approach is applicable to any type of spherical sampling strategy. Accuracy and stability improvements with respect to the previous methods have been demonstrated using near field simulation and far field measurements of various types of antennas.

The translation of the AUT is another mean that could be harnessed to further improve the sparsity of the spherical harmonic spectrum. This significant work goes beyond the scope of this paper and is left for future studies.

References

[1] J. Hald, J. Hansen, F. Jensen, and F. Larsen, *Spherical Near Field Antenna Measurements*, J. Hansen, Ed. Peter Peregrinus, 1988.

[2] R. Cornelius, D. Heberling, N. Koep, A. Behboodi, and R. Mathar, "Compressed sensing applied to spherical near-field to far-field transformation." Davos: Eur. Conf. Antennas Propag. (EuCAP), 2016.

[3] D. Loschenbrand and C. Mecklenbrauker, "Fast antenna characterization via a sparse spherical multipole expansion." Aachen: 4th International Workshop on Compressed Sensing Theory and its Applications to Radar, Sonar and Remote, 2016.

[4] B. Fuchs, L. Le Coq, S. Rondineau, and M. Migliore, "Fast antenna far field characterization via sparse spherical harmonic expansion," *IEEE Trans. Antennas Propag.*, vol. 65, no. 10, pp. 5503–5510, Oct. 2017.

[5] B. Hofmann, O. Neitz, and T. F. Eibert, "On the minimum number of samples for sparse recovery in spherical antenna near-field measurements," *IEEE Trans. on Antennas and Propag.*, July 2019.

[6] N. Mézières, B. Fuchs, L. Le Coq, J.-M. Lerat, R. Contreres, and G. L. Fur, "On the application of sparse spherical harmonic expansion for fast antenna far field measurements," *IEEE Antennas and Wireless Propagation Letters*, 2020.

[7] "IEEE recommended practice for near-field antenna measurements," *IEEE Std 1720-2012*, pp. 1–102, 2012.

[8] F. Jensen and A. Frandsen, "On the number of modes in spherical wave expansions," in *AMTA Proceedings*, 2004.

[9] R. Cornelius and D. Heberling, "Spherical wave expansion with arbitrary origin for near-field antenna measurements," *IEEE Transactions on Antennas and Propagation*, vol. 65, no. 8, pp. 4385–4388, Aug 2017.

[10] C. Culotta-Lopez, K. Wu, and D. Heberling, "Radiation center estimation from near-field data using a direct and an iterative approach," in *AMTA Proceedings*, 2017.

[11] M. Elad, *Sparse and Redundant Representations - From Theory to Applications in Signal and Image Processing*. Springer, 2010.

[12] E. van den Berg and M. P. Friedlander, "Probing the pareto frontier for basis pursuit solutions," *SIAM Journal on Scientific Computing*, vol. 31, no. 2, pp. 890–912, 2008.

[13] ——, "SPGL1: A solver for large-scale sparse reconstruction," June 2007.

[14] D. L. Donoho and J. Tanner, "Precise undersampling theorems," *Proceedings of the IEEE*, vol. 98, no. 6, pp. 913–924, June 2010.

[15] L. C. Biedenharn, J. D. Louck, and P. A. Carruthers, *Angular Momentum in Quantum Physics: Theory and Application*, ser. Encyclopedia of Mathematics and its Applications. Cambridge University Press, 1984.

[16] C. Rasmussen and C. K. I. Williams, *Gaussian Processes for Machine Learning (Adaptive Computation and Machine Learning)*. The MIT Press, 2005.

[17] C. Diallo, "Study and design of new multibeam antenna architectures in Ku and Ka bands for broadband satellite communication applications," Ph.D. dissertation, University of Rennes 1, 2016.